Catalysis Today 178 (2011) 25–33

Contents lists available at ScienceDirect

Catalysis Today

journal homepage: www.elsevier.com/locate/cattod

Steam reforming of glycerol over Ni/Al_2O_3 catalyst

Chin Kui Cheng, Say Yei Foo, Adesoji A. Adesina*

Reactor Engineering and Technology Group, School of Chemical Engineering, The University of New South Wales, Sydney NSW 2052, Australia

ARTICLE INFO

Article history:
Received 2 May 2011
Received in revised form 7 July 2011
Accepted 12 July 2011
Available online 20 August 2011

Keywords:
Glycerol steam reforming
Hydrogen production
Kinetic analysis
Nickel catalyst

ABSTRACT

Glycerol steam reforming has been investigated in a 10-mm ID fixed-bed reactor containing Ni/Al_2O_3 catalyst using a wide range of the steam-to-carbon ratio ($1.1 \leq STCR \leq 4.0$) at temperatures between 723 K and 823 K. Physicochemical characterization revealed that the catalyst surface was populated by both weak and strong acid and basic sites although the catalyst appeared to have a net surface acidity. H_2, CO_2 and CO were the main gaseous products with H_2:CO_2 ratio at approximately 2.15 while H_2:CO ratio varied between 6.0 and 16.0 depending on the reactant feed composition. The specific glycerol consumption rate exhibited fractional reaction orders with respect to both glycerol (0.48) and steam (0.34) and activation energy of about 60 kJ mol^{-1}. Mechanistic considerations indicated that glycerol and steam underwent associative and dissociative adsorption, respectively on two different sites with the surface reaction being the rate-determining step. Additionally, carbon deposition has a positive dependency on the glycerol partial pressure, but it was inhibited in the presence of steam.

1. Introduction

The use of biomass as potential energy provider has gained more prominence in light of high crude oil price. Current world annual energy consumption derived from biomass (renewable source) only represents 14% with the rest coming from coal, electricity and gases [1]. The conversion of biomass to bio-fuels and other value-added chemicals proceeds via different chemistries including esterification, acid hydrolysis, gasification, thermal pyrolysis and steam reforming to syngas [2–10].

In recent years, a considerable amount of research effort has been invested in the area of aqueous or vapour-reformation of oxygenated hydrocarbons [11–22]. Theoretical consideration alone indicates that the reforming of oxygenated hydrocarbons is less energy-intensive than that of the hydrocarbons of similar carbon number. For example, the steam reforming of propane (C_3H_8) has $\Delta G^\circ_{823\,K} = 2.2$ kJ mol^{-1} ($K_{eq} = 0.73$) [23] while the steam reforming of glycerol ($C_3H_8O_3$) has a much lower value, $\Delta G^\circ_{823\,K} = -309.3$ kJ mol^{-1} ($K_{eq} = 4.2 \times 10^{19}$). For hydrocarbons, both carbon–oxygen and hydrogen–oxygen bonds have to be formed. In contrast, oxygenated fuels contain these bonds already and tend to react more easily [24].

Glycerol, a non-edible oxygenated hydrocarbon, is a by-product of biodiesel synthesis and currently over-supplied to the world market due to its limited commercial exploitation. As part of green process engineering (the principle of low-pollutant discharge), the conversion of waste glycerol to the high value-added products is a desirable loop closure step in biodiesel processing plants. Dumesic and co-workers have shown that H_2 may be produced from various carbohydrates employing aqueous phase reforming [25,26]. The present work examines the steam reforming of glycerol, thus, the pertinent reaction is:

$$C_3H_8O_3(g) + 3H_2O(g) \leftrightarrow 3CO_2(g) + 7H_2(g) \quad (1)$$

Reaction in Eq. (1) may be viewed as the combination of the glycerol decomposition (cf. Eq. (2)) and water–gas-shift reaction (cf. Eq. (3)):

$$C_3H_8O_3(g) \leftrightarrow 3CO(g) + 4H_2(g) \quad (2)$$

$$CO(g) + H_2O(g) \leftrightarrow CO_2(g) + H_2(g) \quad (3)$$

These may also be accompanied by other reactions as shown in Eqs. (4)–(10).

$$C_3H_8O_3(g) + 5H_2(g) \leftrightarrow 3CH_4(g) + 3H_2O(g) \quad (4)$$

$$CO(g) + 3H_2(g) \leftrightarrow CH_4(g) + H_2O(g) \quad (5)$$

$$CO_2(g) + 4H_2(g) \leftrightarrow CH_4(g) + 2H_2O(g) \quad (6)$$

$$CO_2(g) + CH_4(g) \leftrightarrow 2CO(g) + 2H_2(g) \quad (7)$$

$$CH_4(g) \leftrightarrow 2H_2(g) + C(s) \quad (8)$$

$$C(s) + H_2O(g) \leftrightarrow CO(g) + H_2(g) \quad (9)$$

$$2CO(g) \leftrightarrow C(s) + CO_2(g) \quad (10)$$

Recent studies have shown that supported Ni catalysts exhibited good glycerol steam reforming activity [27–34]. From a practical standpoint, Ni-based catalyst has a strong appeal since it has been

---

* Corresponding author. Tel.: +61 2 9385 5268; fax: +61 2 9385 5966.
E-mail address: a.adesina@unsw.edu.au (A.A. Adesina).

0920-5861/$ – see front matter © 2011 Elsevier B.V. All rights reserved.
doi:10.1016/j.cattod.2011.07.011

widely used in the petroleum and natural gas processing industries [35,36], hence, the rationale for its application to glycerol steam reforming as part of process development initiatives in commercial biosyngas production.

In the present paper, we report results of experimental studies to measure the rates of H_2, CO_2, CO and CH_4 production from glycerol over alumina-supported Ni catalyst. Rate data were collected at various temperatures and different steam-to-carbon ratios (STCR) and used to infer plausible mechanism governing the glycerol steam reforming reaction under typical experimental conditions.

2. Experimental

2.1. Catalysts preparation and characterization

The nickel nitrate for catalyst preparation was obtained from Sigma Aldrich. The support, γ-Al_2O_3, in pellet form was purchased from Saint Gobain NorPro (USA). All solutions for catalyst preparation throughout this study utilized distilled and deionised pure water generated by NANOpure Diamond UV unit (Barnstead International). Glycerol used (99.5% purity) was obtained from Ajax Finechem (Sydney, Australia). The catalyst was prepared via wet impregnation technique on the commercial alumina using $Ni(NO_3)_2{\cdot}6H_2O$ as the Ni precursor. The metal nitrate solution was added to crushed and sieved alumina particles (140–425 μm) which had been previously calcined at 873 K for 6 h. The resulting slurry was left under constant stirring for 3 h at room temperature. Impregnated catalyst was oven-dried at 403 K for 12 h and cooled to room temperature. Subsequently, the dried catalyst was sieved, ground and calcined in flowing dry air at 873 K for 4 h using a heating rate of 5 K min^{-1}. Calcined catalyst (15 wt.% Ni/Al_2O_3) was finally sieved to 90–140 μm particle size for reaction study.

The BET surface area and pore-size distribution of the calcined sample were determined from N_2 physisorption at 77 K in a Quantachrome Autosorb unit. Prior to the analysis, the fresh catalyst was pre-treated under vacuum condition at 573 K for at least 3 h. Powder X-ray diffraction (XRD) pattern of the calcined catalyst was obtained on X'pert Pro Multi-purpose X-ray Diffraction (MPD) system using Cu Kα radiation ($\lambda = 0.154$ nm) operated at 40 mA and 45 kV. The diffractogram was analysed using X'Pert ScorePlus software. Crystallite size was calculated using Scherrer equation, $d = 0.94\lambda/(\beta\cos\theta)$, where d is the crystallite size, λ is the wavelength of the radiation, β is the full-width at half maximum (FWHM) of the diffraction peak and θ is the diffraction half angle.

The metal dispersion and acid–base properties of the catalyst were obtained using Micromeritics 2910 unit (Micromeritics Instrument Corp.). The calcined catalyst was pre-reduced in situ at 873 K using pure H_2 at a ramping of 1 K min^{-1}. For the pulse H_2-chemisorption runs, the system was purged for 30 min with N_2, and then cooled down to room temperature. Subsequently, the temperature was increased at a constant rate of 2 K min^{-1} to 383 K in 40 ml min^{-1} flow of 10% H_2 in N_2 carrier gas, and held there for 30 min to ensure stable background TCD signal. Finally, a series of 1-cm^3 hydrogen doses at periodic intervals of 5 min were injected into the solid catalyst. The composition of hydrogen-containing gas exiting the system was continuously monitored by the TCD detector. The pulse injection was typically stopped after 13 cycles. Data from H_2 chemisorption was used to estimate metal dispersion. The acid–base properties of the catalyst were evaluated from temperature-programmed desorption (TPD) employing NH_3 and CO_2 as probe gases, respectively. NH_3 adsorption was performed at 423 K using 10% NH_3 in N_2 balance, while CO_2 adsorption was carried out using 10% CO_2 in He at 323 K. Adsorption was carried out for 1 h to ensure complete coverage of the catalyst surface with the probe molecules followed by purging at the same adsorption temperature with carrier gas (N_2 or He) for 30 min at 40 ml min^{-1}. The purging step was implemented to ensure removal of any excess or physically bound NH_3 or CO_2 molecules. Temperature-programmed desorption was then commenced at a constant heating rate up to 873 K for NH_3-TPD or 973 K for CO_2-TPD and then maintained at that level for 60 min. During this step, the outlet stream was monitored by a TCD detector and recorded. The sample was then cooled to 423 K for NH_3-TPD or 323 K for CO_2-TPD, and then allowed to equilibrate before resaturating the surface with NH_3 or CO_2 for 60 min, followed by purging for 60 min. The cycle was then repeated on each occasion with a different heating rate value, The determination of heat of desorption, $-\Delta H_{desorption}$ from TPD experiments is given by:

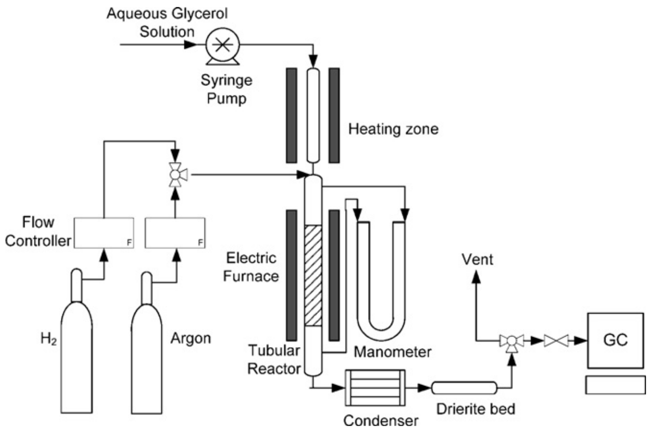

Fig. 1. Schematic diagram of the experimental setup.

$$\ln\frac{\beta}{T_p^2} = \frac{(-\Delta H_{desorption})}{RT_p} + \ln\frac{(-\Delta H_{desorption})A_{sat}}{RC} \qquad (11)$$

where β is the heating rate (K min^{-1}), $-\Delta H_{desorption}$ is the heat of desorption (kJ mol^{-1}), R is the universal gas constant, T_p is the peak temperature (K), A_{sat} is quantity adsorbed at saturation and C is the constant related to the desorption rate. From Eq. (11), a plot of $\ln\beta/{T_p}^2$ against $1/T_p$ will produce a linear slope $(-\Delta H_{desorption}/R)$ from which the value of heat of desorption $(-\Delta H_{desorption})$ of adsorbed gas species may be determined.

Thermogravimetric analysis of the calcination and reduction characteristics of fresh catalyst was performed using a ThermoCahn TG 2121 system. Temperature-programmed calcination was carried out at 873 K, for 5 h, with heating rates of 5, 10 and 20 K min^{-1} using 55 ml min^{-1} high purity air. Temperature programmed reduction (TPR) of the oxide catalyst was performed up to 973 K, for 5 h, at 5 K min^{-1} with 50% H_2/Ar mixture (55 ml min^{-1}).

2.2. Experimental apparatus and catalytic activity evaluation

Glycerol steam reforming reaction experiments were conducted in a stainless-steel fixed bed reactor with 10 mm *i.d.* (cf. Fig. 1) at atmospheric pressure and reaction temperature of 723–823 K. Catalyst bed was supported by quartz wool at the bottom end of the reactor. Glycerol–water mixture with composition 30–60 wt.% glycerol (corresponding to the steam-to-carbon ratio, STCR of 1.1–4.0) was used as feed to ensure stoichiometrically excess steam. The mixture was pumped with a 50 ml motorised syringe (Razel Scientific Instruments, model A-99) directly into the vaporizer upstream of the reactor (at 773 K), and then downwards into the reactor after being mixed with inert Ar to a total flow rate of 5.0×10^4 ml ${g_{cat}}^{-1}$ h^{-1}. Prior to reaction, the catalyst was reduced in flowing H_2 (50 ml min^{-1} STP) for 2 h. Heating rate was controlled at 10 K min^{-1}. The bed pressure drop was always below 3 kPa as

Table 1
Physicochemical properties of Al_2O_3 support and fresh metal-Al_2O_3 catalysts.

Properties		Fresh Al_2O_3	Calcined Al_2O_3	Ni/Al_2O_3
BET surface area ($m^2\,g^{-1}$)		228.6	210.6	175.1
Pore volume ($ml\,g^{-1}$)		0.71	0.69	0.57
Dispersion (%)		–	–	4.27
Metal surface area ($m^2\,g^{-1}$)		–	–	4.3
Metal particle diameter (nm)		–	–	23.7
NH_3 desorption energy, ΔH_{NH_3} (kJ mol^{-1})	Peak I	–	68.9	48.3
	Peak II	–	–	79.7
CO_2 desorption energy, ΔH_{CO_2} (kJ mol^{-1})	Peak I	–	63.2	62.6
	Peak II	–	68.4	46.7
Acid site concentration (μmol m^{-2})	Peak I	–	2.1	0.43
	Peak II		N/A	2.0
Basic site concentration (μmol m^{-2})	Peak I	–	0.14	0.21
	Peak II		0.32	0.29
Acidic: basic site ratio	Peak I	–	15.4	2.0
	Peak II		N/A	7.0

measured by a U-tube water manometer. All inlet gas flow rates were controlled by Brooks 5850E Series electronic mass flow controllers. Reactor outlet gases passed through a cold trap for liquid products capture and then over a drierite ($CaSO_4$) bed (8 mesh). The exit gas composition was measured using a Shimadzu GC–8A equipped with a Haysep DB column (9 m × 3.18 mm × 2.16 mm SS, 100/120 mesh) maintained at 393 K and a thermal conductivity at 423 K. Ar was used as carrier gas. Outlet flow rate of dried gas was measured using a bubble meter.

In order to minimize transport-induced conditions [37], the ratio of the catalyst bed length to particle diameter (L/D_p) was 80, catalyst particle size between 90 and 140 μm and gas hourly space velocity (GHSV) of 5.0×10^4 ml $g_{cat}{}^{-1}$ h^{-1} were employed. Preliminary runs with flow rate variation (50–200 ml min^{-1}) and particle size range 45–425 μm (covering 4 different cuts) analysed in the conventional sense [37] confirmed that these conditions were adequate for transport-free rate data collection.

The catalytic performance was evaluated in terms of conversion into gaseous products selectivity and yield which are defined as

Glycerol conversion:

$$X_G = \frac{F_{CO_2} + F_{CO} + F_{CH_4}}{3 \times \text{molar flow rate of glycerol in the feed}} \times 100 \qquad (12)$$

Yield and selectivity of the carbon-containing product s are defined as:

$$Y_i = \frac{F_i}{3 \times \text{molar flow rate of glycerol in the feed}} \times 100 \qquad (13a)$$

$$S_i = \frac{F_i}{F_{CO_2} + F_{CO} + F_{CH_4}} \times 100 \qquad (13b)$$

where i = CO_2, CO and CH_4.

Yield and selectivity of H_2 are defined as:

$$Y_{H_2} = \frac{2 \times F_{H_2}}{[(8 \times \text{molar feed flow rate of glycerol}) + (2 \times \text{molar feed flow rate of water})]} \times 100 \qquad (14a)$$

$$S_{H_2} = \frac{2 \times F_{H_2}}{\left[8/3 \times (F_{CO_2} + F_{CO} + F_{CH_4}) + 2 \times (\text{molar rate of water consumed})\right]} \times 100 \qquad (14b)$$

where F_i is the molar flow rate (mol s^{-1}) of species i. Since water was removed prior to GC analysis, the last term of the denominator in Eq. (14b) was neglected in the estimation of H_2 selectivity and hence, in some situations values greater than 100% were obtained as later discussed in Section 3.2.3. The total organic carbon (TOC) analysis of the used catalyst after each run was performed on a Shimadzu TOC Analyzer SM-5000A using ultrapure (>99.9%) oxygen and temperature of 1173 K.

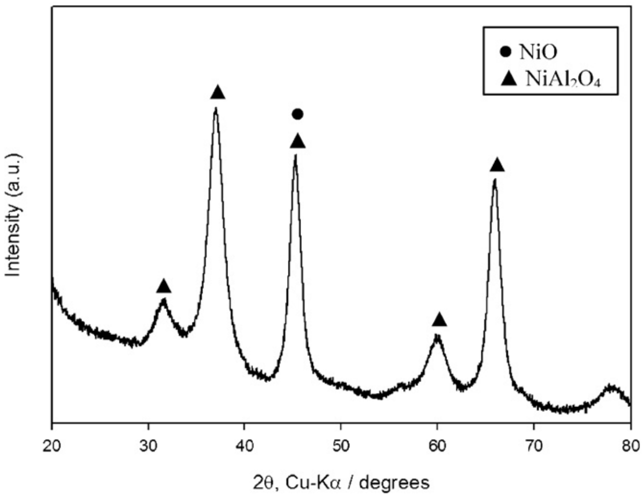

Fig. 2. XRD pattern of the calcined Ni/Al_2O_3 catalyst.

3. Results and discussion

3.1. Catalyst characterization

Table 1 shows that the BET area and pore volume for the fresh Ni/Al_2O_3 catalyst were smaller than the corresponding values for the calcined alumina support due to pore blockage by the impregnation of metal oxide particles. H_2 chemisorption analysis showed a Ni particle size of 24 nm with dispersion of 4.3%. In addition, the metal surface area is 4.3 m^2 $g_{cat}{}^{-1}$ as displayed in Table 1. These results were nearly identical to those obtained by Osaki and Mori [38] and Natesakhawat et al. [39] for the same Ni/Al_2O_3 catalyst system. Fig. 2 shows XRD diffraction pattern of Ni/Al_2O_3 catalyst. The diffractogram shows a strong formation signal for $NiAl_2O_4$ at angle $2\theta = 37°$ (3 1 1), 45° (4 0 0) and 66° (4 4 0). The NiO (1 1 1) phase at 43.3° has probably been overlapped by the $NiAl_2O_4$ (4 0 0) signal at 45° since the latter peak began at 42.9° and ended at 47°.

CO_2-TPD showed two distinct peaks (cf. Fig. 3) indicating two different basic sites. Analysis of the data at different heating rates gave the heat of desorption 62.6 kJ mol^{-1} for Peak I (located

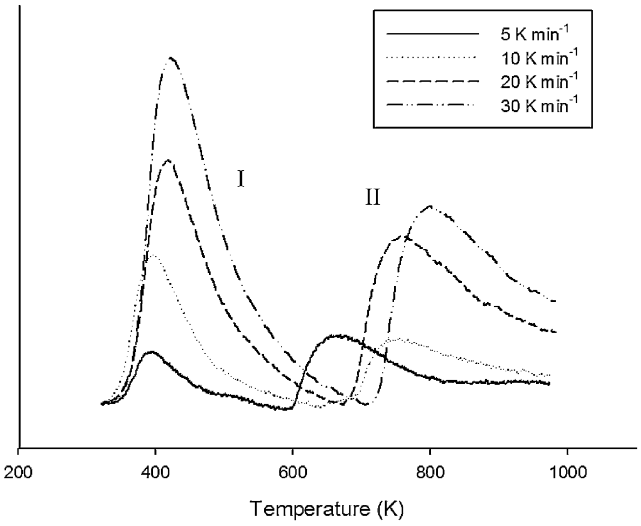

Fig. 3. CO_2-TPD performed on Ni/Al_2O_3.

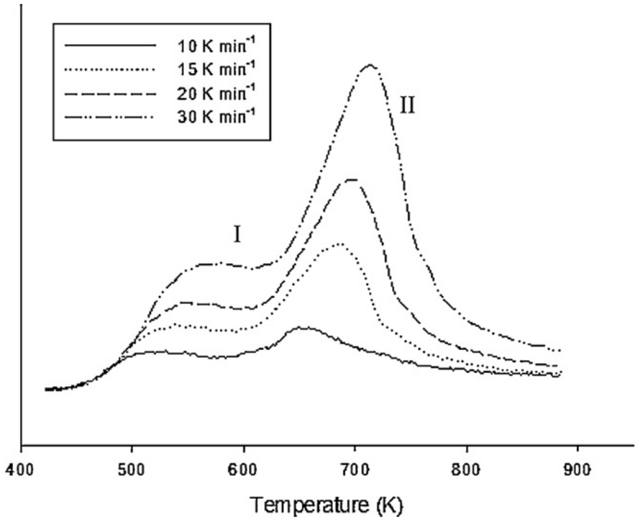

Fig. 4. NH_3-TPD performed on Ni/Al_2O_3.

Table 2
Summary of criteria used for determining external and pore transport limitations.

	External	Internal
Mass	$\frac{(-r_{\exp})\rho_b d_p \lvert n \rvert}{k_c C_{Ab}} < 0.15$	$\phi^2_{\exp} = \frac{(-r_{\exp}) d_p^2 \rho_b}{4 D_{\text{eff}} C_{As}} < 1$
Heat	$\frac{(-\Delta H_{rxn})(-r_{\exp})\rho_b d_p E_{\text{act}}}{h T_b^2 R} < 0.15$	$\left\lvert \frac{(-\Delta H_{rxn}) d_p^2 \rho_b (-r_{\exp}) E_{\text{act}}}{\lambda_{\text{eff}} R T_s^2} \right\rvert < 3$

k_c is obtained from $J_D = k_c/U(\text{Sc})^{2/3}$ where $\varepsilon J_D = (0.765/\text{Re}^{0.82}) + (0.365/\text{Re}^{0.386})$, $\text{Sc} = \mu/\rho_g D_{\text{AB}}$ and $\text{Re} = \rho U d_p/\mu$; ε is the void fraction estimated at 0.38 using the equation $\rho_b = (1-\varepsilon)\rho_c$; and $D_{\text{eff}} = 0.1 \times D_{\text{AB}}$ where D_{AB} is estimated using Fuller–Schettler–Giddings equation [42] as $0.45 \times 10^{-4}\ \text{m}^2\ \text{s}^{-1}$ at 823 K. The heat transfer coefficient h is estimated from $J_H = J_D = (h/C_{p_{\text{mix}}} G)(Pr)^{2/3}$ where J_H is the heat transfer J-factor and Pr is the Prandtl number, $Pr = C_{p_{\text{mix}}} \mu/\lambda_g$ while $\lambda_{\text{eff}} = 10 \times \lambda_g$.

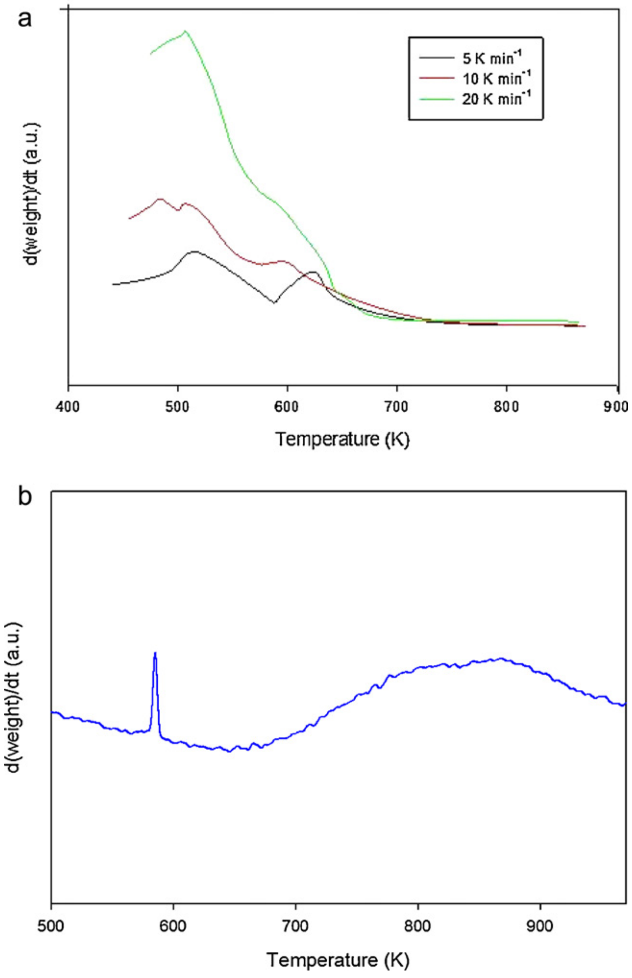

Fig. 5. (a) Derivative weight loss curves for temperature-programmed calcination of the catalyst at different heating rates. (b) Derivative weight loss curves for TPR at 5 K min^{-1}.

between 398 and 428 K) and 46.7 kJ mol^{-1} for Peak II (673–803 K). The lower temperature peak is indicative of the presence of weak basic site while Peak II is probably due to a strong basic site. The presence of two distinct peaks was also observed for NH_3-TPD analysis as shown in Fig. 4, *viz.*; a weak acid centre in the low temperature region (533–578 K) and a high temperature peak (663–708 K) indicative of a strong acid site. The heat of desorption for NH_3 was estimated as 48.3 and 79.7 kJ mol^{-1} for Peaks I and II, respectively. Similar NH_3-TPD analysis on calcined alumina support revealed the presence of weak acid site only while both weak and strong basic sites were present on calcined alumina support (cf. Table 1). This indicates that the strong acid site was most likely located at the interface of metal–alumina support while basic site for Ni/Al_2O_3 catalyst may be due to the presence of surface hydroxyl and interstitial hydroxyl species in the alumina support.

The derivative weight loss curves for the catalyst during temperature-programmed calcination (TPC) are shown in Fig. 5a and that for TPR in Fig. 5b. The TPC curves revealed that the metal nitrate decomposition to oxides took place below 723 K regardless of the heating rate. The first peak centred at approximately 513 K may be attributed to the formation of Ni_2O_3:

$$2\text{Ni}(\text{NO}_3)_2 \rightarrow \text{Ni}_2\text{O}_3 + 2\text{NO} + 2\text{NO}_2 + 3/2\text{O}_2 \tag{15a}$$

However, the subordinate peak at 493 K for the run using a heating rate of 10 K min^{-1} suggests the possibility that Ni nitrate decomposition may also produce Ni_3O_4 [40] via the companion equation;

$$3\text{Ni}(\text{NO}_3)_2 \rightarrow \text{Ni}_3\text{O}_4 + 3\text{NO} + 3\text{NO}_2 + 5/2\text{O}_2 \tag{15b}$$

Table 3
Comparison of product distributions obtained experimentally and at thermodynamic equilibrium.

Temperature (K)	Experimental[a]				Equilibrium conditions[b] (mol of product/mol of glycerol)			
	H_2	CO_2	CO	CH_4	H_2	CO_2	CO	CH_4
823	3.3	1.6	0.28	0.23	4.8	2.2	0.40	0.45
773	1.5	0.72	0.16	0.072	3.5	2.0	0.25	0.80
723	1.0	0.47	0.069	0.017	2.6	1.7	0.10	1.1

[a] $F_i/F_{glycerol}$.
[b] Estimated using the method proposed by Adhikari et al. [43] and Rossi et al. [44]. Thermochemical properties taken from Yaws [45].

Table 4a
Selectivity and yield of individual products as function of $P_{glycerol}$ (P_{steam} = 57.0 kPa) at reaction temperature of 823 K.

$P_{glycerol}$ (kPa)	X_G (%)	Selectivity (%)				Yield (%)			
		H_2	CO_2	CO	CH_4	H_2	CO_2	CO	CH_4
4.8	79.8	137.0	83.8	11.0	5.2	27.4	66.9	8.8	4.1
7.5	71.3	119.0	76.0	13.1	10.9	29.1	54.2	9.3	7.8
11.2	61.7	102.0	67.7	17.3	15.1	27.5	41.8	10.7	9.3
16.7	54.2	92.1	60.2	21.6	18.2	27.0	32.6	11.7	9.9

Table 4b
Selectivity and yield of individual products as function of P_{steam} ($P_{glycerol}$ = 7.4 kPa) at reaction temperature of 823 K.

P_{steam} (kPa)	X_G (%)	Selectivity (%)				Yield (%)			
		H_2	CO_2	CO	CH_4	H_2	CO_2	CO	CH_4
25.2	56.8	123.0	67.0	21.1	8.9	37.6	39.7	12.0	5.1
37.8	64.3	121.0	73.0	17.0	10.0	34.2	46.9	10.9	6.4
56.7	71.3	119.0	76.0	13.1	10.9	29.1	54.2	9.3	7.8
88.3	82.9	119.0	80.7	9.4	9.9	24.7	67.0	7.8	8.2

Table 5
Estimates of parameters for glycerol steam reforming (nonlinear least squares).

Major product	k (10^6) at 823 K mol m^{-2} s^{-1} $kPa^{-(\beta_{glycerol}+\beta_{steam})}$	$\beta_{glycerol}$	β_{steam}
$C_3H_8O_3$	0.61	0.48	0.34
H_2	5.6	0.34	0.27
CO_2	1.4	0.39	0.41
CO	6.3	0.74	−0.39
CH_4	0.081	0.88	0.34

The broad shoulder peak (570–723 K) corresponds to further oxide decomposition, namely;

$$Ni_2O_3 \rightarrow 2NiO + ½O_2 \tag{15c}$$

The formation of a $NiAl_2O_4$ phase was the result of the solid–solid reaction between NiO and the Al_2O_3 support [41] at temperature greater than 723 K where all the TPC curves were flat since it was not accompanied by a weight change.

$$NiO + Al_2O_3 \rightarrow NiAl_2O_4 \tag{15d}$$

The H_2 TPR spectra in Fig. 5b shows reduction peaks centred at 585 K (NiO to Ni) and 853 K ($NiAl_2O_4$ to Ni/Al_2O_3). This is shown as:

$$NiO + H_2 \rightarrow Ni + H_2O \tag{16a}$$

$$NiAl_2O_4 + H_2 \rightarrow Ni + Al_2O_3 + H_2O \tag{16b}$$

3.2. Reaction studies

3.2.1. Mass and heat transport limitations

Meaningful kinetic data is only obtainable in the region of negligible mass and heat transport limitations. Hence, preliminary runs were conducted at the highest reaction temperature to evaluate the possibility of transport intrusions. The external and pore diffusional resistances were computed using criteria presented in Table 2. Substitution of the relevant values into the left-hand side of these criteria gave values of the order of 10^{-3} while the Thiele modulus, ϕ was 0.012. These results confirmed the absence of external and internal transport limitations.

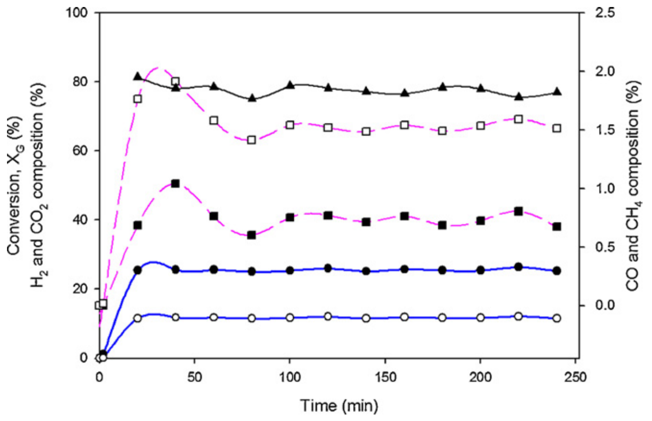

Fig. 6. The transient profiles of glycerol conversion X_G (▲) and dry composition of H_2 (●), CO_2 (○), CO (□) and CH_4 (■) in glycerol steam reforming. Conditions: 823 K; $P_{glycerol}$ = 4.8 kPa, P_{steam} = 57.0 kPa; GHSV = 5.0 × 10^4 ml g_{cat}^{-1} h^{-1} (STCR at 4.0).

3.2.2. Evaluation of experimental data against thermodynamic equilibrium

Apart from transport effects, it is important that the composition data collected for kinetic analysis be reasonably far from those obtainable under equilibrium conditions. Adhikari et al. [43] and Rossi et al. [44] have provided a thermodynamic assessment of the product distribution for glycerol steam reforming using the non-stoichiometric method. In the current validation, data collected at STCR ≈ 2.6 and temperatures between 723 and 823 K (expressed as molar flow rate of product over molar flow rate of glycerol at inlet) were employed and compared to the equilibrium product distribution. As shown in Table 3, experimental product distri-

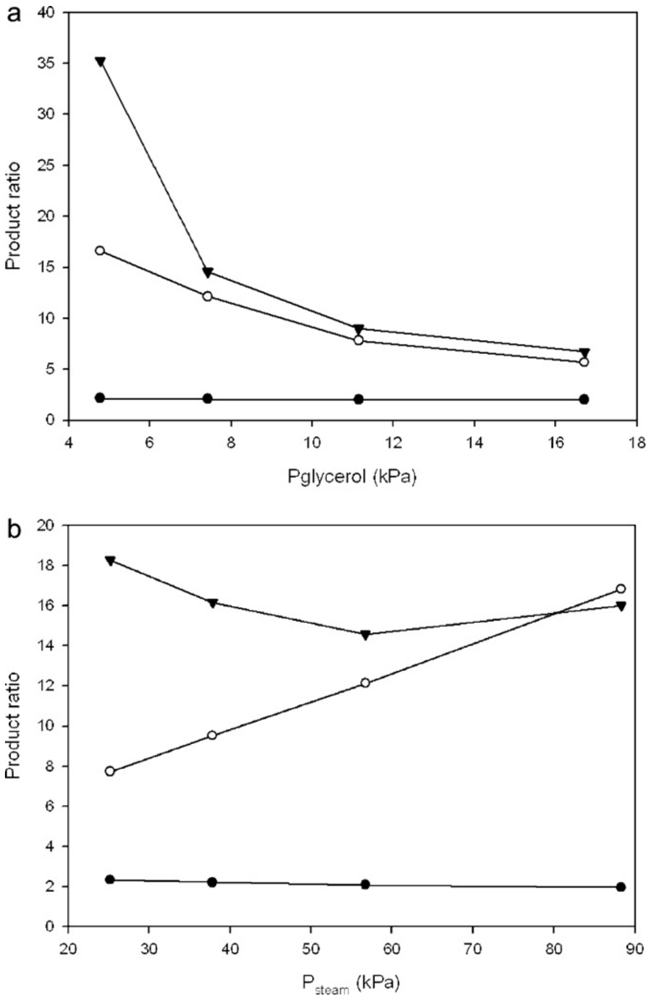

Fig. 7. (a) Product ratio of H_2:CO_2 (●), H_2:CO (○) and H_2:CH_4 (▼) as function of $P_{glycerol}$ (P_{steam} = 57.0 kPa) at reaction temperature of 823 K. (b) Product ratio of H_2:CO_2 (●), H_2:CO (○) and H_2:CH_4 (▼) as function of P_{steam} ($P_{glycerol}$ = 7.4 kPa) at reaction temperature of 823 K.

butions (H_2, CO_2, CO and CH_4) are smaller than the equilibrium product composition at the temperatures used. This indicates that the rate data collected during glycerol reforming condition were sufficiently far from the thermodynamic equilibrium and would be useful for kinetic interpretation.

3.2.3. *Catalytic activity*

The transient profiles showing glycerol conversion and the product composition at 823 K (30 wt.% glycerol) is presented in Fig. 6. Blank tests using the same feed and either an empty reactor tube or calcined Al_2O_3 particles in lieu of the catalyst yielded negligible glycerol conversion. This suggests that neither the homogenous gas phase glycerol decomposition nor the alumina support contributed to the observed activity of the Ni catalyst. Given that the calcined alumina and the Ni/Al_2O_3 catalyst have similar acid centres with the exception of the strong acid site due to Ni impregnation, it would seem that the active site for glycerol reforming was the reduced Ni atom. GC analysis revealed that the main gaseous products were H_2, CO_2, CO and CH_4. Previous work by other researchers also indicated that above reaction temperature of 673 K, H_2, CO_2, CO and CH_4 were the only products of glycerol steam reforming [15,19,27].

The glycerol conversion (X_G) history in Fig. 6 is essentially flat suggesting that glycerol consumption rate attained a relatively quick steady-state (within about 1 h on-stream) probably due to rapid adsorption of glycerol on the catalyst surface. However, individual products exhibited different transient profiles. The formation profiles for H_2 and CO_2 revealed a rise to steady-state composition within the first 30 min and thereafter remained invariant with time while the transient profiles for both CO and CH_4 showed an initial peak before levelling off. The initial overshoot in the CO profile indicates a relatively fast decomposition of glycerol to CO and H_2 (cf. Eq. (2)). Under stoichiometrically excess steam conditions employed in this study, a significant fraction of the original CO was consumed via the WGS (Eq. (3)) to yield CO_2 and additional H_2. The latter may then further take part in the hydrogenolysis of glycerol to produce CH_4 as implicated by Eq. (4). The drop in CO after attaining a peak was due to loss via the WGS while CH_4 relaxation to a steady-state value was probably due to dehydrogenation to surface carbonaceous species and H_2. Both glycerol hydrogenolysis and CH_4 dehydrogenation are thermodynamically feasible under reaction conditions. Indeed, total organic carbon content (TOC) analysis of the used catalysts (as later discussed) also lends credence to this proposition. The data in Fig. 6 indicate a steady-state product ratio H_2:CO_2 of 2.17 which compares favourably with the stoichiometric H_2:CO_2 ratio of 2.33.

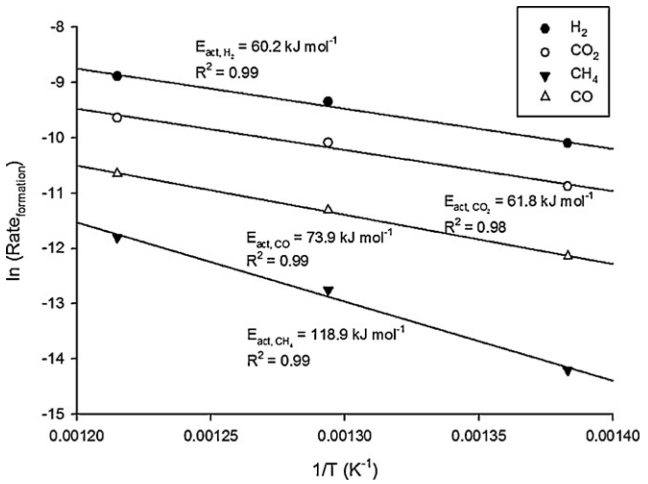

Fig. 8. Arrhenius plots for data collected at inlet partial pressures of $P_{glycerol}$ = 7.4 kPa and P_{steam} = 57.0 kPa (STCR at 2.6).

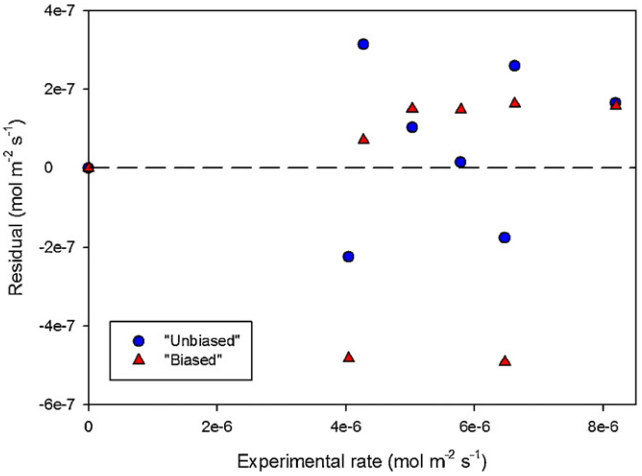

Fig. 9. Example of "unbiased" and "biased" plots for residual plot. Data collected at 823 K.

Tables 4a and 4b list the variation of product distribution with partial pressure of both reactants and reaction temperature. In the presence of excess steam, H_2 and CO_2 always formed the bulk of

Table 6
Kinetic parameters calculated from the rate equation based on the power-law.

Pre-exponential factor A (mmol m^{-2} s^{-1})					E_{act} (kJ mol^{-1})				
$C_3H_8O_3$	H_2	CO_2	CO	CH_4	$C_3H_8O_3$	H_2	CO_2	CO	CH_4
3.81	37.2	11.6	308.6	2834.2	59.8	60.2	61.8	73.9	118.9

Table 7
Model discrimination criteria.

Statistical consideration	Parameters/correlations involved	Remarks
Parity plot	$\theta = \tan^{-1} y$ where y is the slope of parity plot	Ideally, θ should be 45°
Residual plot		An unbiased residual plot shows uniform scattered residual data points without particular trend as shown in Fig. 10
MDC analysis	$\mathrm{MDC} = \frac{\sum (r_i - \bar{r})^2}{\sum (r_i - r_i^{\mathrm{predicted}})^2} - \frac{2P}{N}$ where MDC, model discrimination criterion r_i, specific reaction rate $\bar{r}$, average specific reaction rate P, no. of parameters involved N, no. of experimental points	MDC ≤ 16: poor fitting MDC ≥ 20: acceptable

Table 8
Reaction parameters estimation from LH-type of equations.

Model	Equation	Variables	Model discrimination				Remarks
			R^2	Parity plot Θ	Residual plot	MDC	
1	$\frac{k_{rxn} P_G P_W}{(1+K_G P_G + K_W P_W)}$	$k_{rxn} = 7.431 \times 10^{-8}$ mol m^{-2} s^{-1} kPa^{-2} $K_G = 0.0685$ kPa^{-1} $K_W = 0.0145$ kPa^{-1}	0.98	44.64°	Unbiased	17.19	Positive kinetic parameters. MDC is relatively low. However, it admits single adsorption site
2	$\frac{k_{rxn} P_G \sqrt{P_W}}{(1+K_G P_G + \sqrt{K_W P_W})}$	$k_{rxn} = 8.481 \times 10^{-8}$ mol m^{-2} s^{-1} kPa$^{-1.5}$ $K_G = 0.1156$ kPa^{-1} $K_W = 0.0422$ kPa^{-1}	0.99	44.67°	Biased	27.46	Positive kinetic parameters. High MDC. However, residual plot is biased.
3	$\frac{k_{rxn} P_W \sqrt{P_G}}{(1+K_W P_W + \sqrt{K_G P_G})}$	$k_{rxn} = 2.558 \times 10^{-7}$ mol m^{-2} s^{-1} kPa$^{-1.5}$ $K_G = 0.0441$ kPa^{-1} $K_W = 0.0013$ kPa^{-1}	0.99	44.80°	Biased	33.40	Positive kinetic parameters. High MDC. However, residual plot is biased.
4	$\frac{k_{rxn} \sqrt{P_G P_W}}{(1+\sqrt{K_G P_G} + \sqrt{K_W P_W})}$	$k_{rxn} = 2.757 \times 10^{-7}$ mol m^{-2} s^{-1} kPa^{-1} $K_G = 0.1105$ kPa^{-1} $K_W = 0.0046$ kPa^{-1}	0.99	44.75°	Biased	36.75	Positive kinetic parameters. High MDC. However, residual plot is biased.
5	$\frac{k_{rxn} P_G P_W}{(1+K_G P_G)(1+K_W P_W)}$	$k_{rxn} = 1.017 \times 10^{-7}$ mol m^{-2} s^{-1} kPa^{-1} $K_G = 7.34 \times 10^{-4}$ kPa^{-1} $K_W = 0.0104$ kPa^{-1}	0.98	44.60°	Unbiased	13.70	Positive kinetic parameters. However, relatively low MDC.
6	$\frac{k_{rxn} P_G \sqrt{P_W}}{(1+K_G P_G)(1+\sqrt{K_W P_W})}$	$k_{rxn} = 1.330 \times 10^{-7}$ mol m^{-2} s^{-1} kPa^{-1} $K_G = 5.60 \times 10^{-4}$ kPa^{-1} $K_W = 0.043$ kPa^{-1}	0.98	44.55°	Unbiased	21.00	Positive kinetic parameters. Model admits adsorption on two different sites.
7	$\frac{k_{rxn} P_W \sqrt{P_G}}{(1+K_W P_W)(1+\sqrt{K_G P_G})}$	$k_{rxn} = 4.142 \times 10^{-7}$ mol m^{-2} s^{-1} kPa^{-1} $K_G = 1.02 \times 10^{-4}$ kPa^{-1} $K_W = 7.65 \times 10^{-4}$ kPa^{-1}	0.99	44.65°	Biased	27.00	Positive kinetic parameters. High MDC. However, residual plot is biased.
8	$\frac{k_{rxn} \sqrt{P_G P_W}}{(1+\sqrt{K_G P_G})(1+\sqrt{K_W P_W})}$	$k_{rxn} = 4.293 \times 10^{-7}$ mol m^{-2} s^{-1} kPa^{-1} $K_G = 2.67 \times 10^{-4}$ kPa^{-1} $K_W = 4.31 \times 10^{-4}$ kPa^{-1}	0.99	44.64°	Biased	27.60	Positive kinetic parameters. High MDC. However, residual plot is poor.

gaseous products. Specifically, Table 4a shows the conversion, X_G, as well as selectivity and yield of product as a function of glycerol partial pressure, P_{glycerol} at a constant steam partial pressure, $P_{\mathrm{steam}} = 57$ kPa. It is apparent that X_G decreased almost linearly with increasing P_{glycerol}, from 80% at $P_{\mathrm{glycerol}} = 4.8$ kPa to 54% at $P_{\mathrm{glycerol}} = 16.7$ kPa. Conversely, Table 4b shows that X_G increased with P_{steam} with X_G of 57% at $P_{\mathrm{steam}} = 25.0$ kPa, rising to 83% at $P_{\mathrm{steam}} = 88.3$ kPa. It is evident from Table 4a that CO_2 yield decreased with increased glycerol partial pressure while the yield of both CO and CH_4 increased within the increasing glycerol partial pressure. The H_2 yield was relatively unchanged probably due to the fact that excess steam was used for all 4 runs. Selectivity value in excess of 100% is simply an artefact of the fact that the amount of H_2 contributed from water appeared in the numerator (cf. Eq. (14b)) but was not reflected in the denominator since the water consumed was not measured during GC analysis and neglected in the computation. Even so, a concomitant increase in CH_4 yield (4–10%) indicated that H_2 was consumed in producing CH_4 (cf. Table 4a) consistent with the hydrogenolysis of glycerol. As indicated in Fig. 7, the ratio of H_2:CO_2, i.e., (r_{H_2}/r_{CO_2}), was found within the narrow window between 2.0 and 2.33 regardless of the reactant partial pressure. Nevertheless, the product H_2:CO ratio decreased from 16.0 to 6.0 as P_{glycerol} increased (cf. Fig. 7a). Interestingly, as shown in Fig. 7a, the H_2:CH_4 ratio decreased with P_{glycerol} as a result of an increase in the yield of CH_4. Table 4b, in particular shows that CO yield decreased while that for CH_4 increased with P_{steam}. This indicates that CH_4 steam reforming is practically nonexistent whereas the drop in CO yield is consistent with loss via WGS as also confirmed by the increase in CO_2 yield with P_{steam}. The anomalous (>100%) values reported for H_2 selectivity has been earlier discussed. Nonetheless, Fig. 7b reveals that the product formation rate ratio, of H_2:CO increased from 8.0 to 17.0 while that for H_2:CH_4 decreased from 18.0 to 15.0. The reduction of H_2:CH_4 ratio with both P_{glycerol} and P_{steam} confirms the earlier proposition that CH_4 was mainly generated from the hydrogenolysis of glycerol.

3.2.4. *Kinetic modelling*

a. Empirical modelling

Glycerol reforming rate was fitted to the power law equation

$$(-r_{\mathrm{GSR}}) = kP_{\mathrm{glycerol}}^{\beta_{\mathrm{glycerol}}} P_{\mathrm{steam}}^{\beta_{\mathrm{steam}}} \quad (19)$$

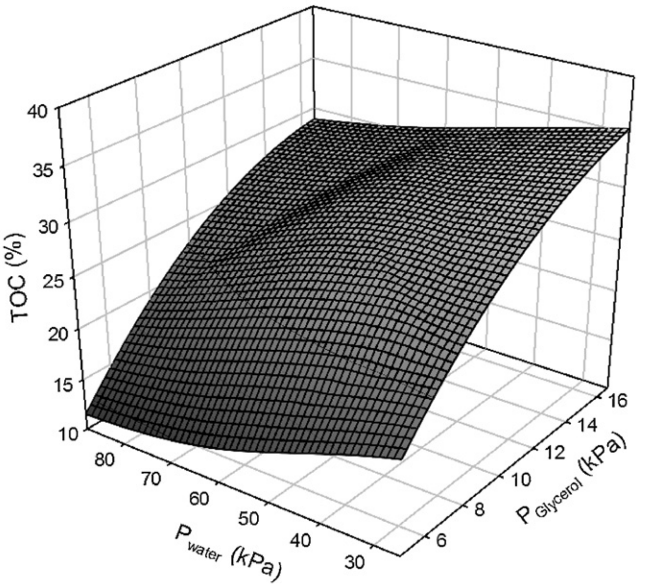

Fig. 10. Amount of total organic carbon deposited on catalyst at 823 K as a function of feed composition.

where $-r_{GSR}$ is the glycerol reforming rate, k is the reforming rate constant, $P_{glycerol}$ and P_{steam} are reactants' partial pressure while $\beta_{glycerol}$ and β_{steam} are the order of reaction. Employing the same power-law model, estimates of the $\beta_{glycerol}$ and P_{steam}-values related to the C_1 species were obtained. Regression of the rate data gave the parameter estimates provided in Table 5 with good regression coefficient ($R^2 \geq 0.99$). All species showed fractional positive dependency on the glycerol. The steam inhibition (negative β value) of CO rate is an indication of either competitive adsorption of steam on the same site as CO (especially at the relatively high steam partial pressure used) or loss of CO produced via WGS reaction to CO_2 as indicated by product yield and selectivity in Table 4b.

The glycerol steam reforming rate data at different temperatures (723 K, 773 K and 823 K) were also used to estimate the activation energy for product formation (cf. Fig. 8). As may be seen from Table 6, CO_2 formation has a lower activation energy, E_A (61.8 kJ mol^{-1}) than that for CO production (74.0 kJ mol^{-1}). The nearly identical activation energy value for glycerol consumption (≈60.0 kJ mol^{-1}) and formation of H_2 and CO_2 (60.2 and 61.8 kJ mol^{-1}, respectively) showed that Eq. (1) was the major source of production for these two species.

b. Mechanistic conjecture

The adsorption of glycerol and steam on the catalyst may be on a similar site or each may adsorb on different surface centres. In particular, the adsorption of OH groups onto strong acid sites is possible, as reported before for glycerol dehydration on acidic catalysts [46,47]. Li et al. [48] reported adsorption of steam on alumina supported metal catalyst for reforming reaction. Therefore, Langmuir–Hinshelwood (LH) kinetic expressions based on single-site or dual-sites adsorption with bimolecular surface reaction as rate-determining step were derived and assessed using the glycerol consumption rate data. A representative reaction mechanism is shown in Eqs. (M1)–(M14).

$$C_3H_8O_3 + X_1 \leftrightarrow C_3H_8O_3\text{-}X_1 \tag{M1}$$

$$H_2O + 2X_2 \leftrightarrow OH\text{-}X_2 + H\text{-}X_2 \tag{M2}$$

$$C_3H_8O_3\text{-}X_1 + H\text{-}X_2 \rightarrow CH_2OHCHOH\text{-}X_1 + CHOH\text{-}X_2 + 2H_2 \tag{M3}$$

$$CHOH\text{-}X_2 \rightarrow CO\text{-}X_2 + H_2 \tag{M4}$$

$$CH_2OHCHOH\text{-}X_1 + H\text{-}X_2 \rightarrow CH_2OH\text{-}X_1 + CH_3O\text{-}X_2 \tag{M5}$$

$$CH_2OH\text{-}X_1 + X_2 \rightarrow CH_2\text{-}X_1 + OH\text{-}X_2 \tag{M6}$$

$$CH_2\text{-}X_1 + H\text{-}X_2 \rightarrow CH_3\text{-}X_1 + X_2 \tag{M7}$$

$$CH_3\text{-}X_1 + H\text{-}X_2 \rightarrow CH_4 + X_1 + X_2 \tag{M8}$$

$$CH_3O\text{-}X_1 + X_2 \rightarrow CH_2O\text{-}X_1 + H\text{-}X_2 \tag{M9}$$

$$CH_2O\text{-}X_1 + X_2 \rightarrow HCO\text{-}X_1 + H\text{-}X_2 \tag{M10}$$

$$HCO\text{-}X_1 + X_2 \rightarrow CO\text{-}X_1 + H\text{-}X_2 \tag{M11}$$

$$CO\text{-}X_1 \leftrightarrow CO + X_1 \tag{M12}$$

$$CO\text{-}X_1 + OH\text{-}X_2 \leftrightarrow CO_2 + H\text{-}X_2 + X_1 \tag{M13}$$

$$H\text{-}X_2 + H\text{-}X_2 \leftrightarrow H_2 + 2X_2 \tag{M14}$$

where X_1 and X_2 are basic and acid active sites, respectively. Model selection was based on the criteria listed in Table 7. Fig. 9 illustrates a typical residual plot. The summary of kinetic parameters and model discrimination outcomes are presented in Table 8 from whence it is evident that Model 6, which was based on dual-site molecular adsorption of glycerol and dissociative adsorption of steam satisfied all the discrimination requirements. Model 6 was also consistent with physicochemical analyses, which revealed that, both acid and basic sites were present on the catalyst surface.

3.3. Characterization of used catalysts

Although the Ni/Al_2O_3 catalyst possesses steam reforming activity, carbon deposition was evident on the used samples. Fig. 10 shows the total organic carbon deposited on Ni/Al_2O_3 catalyst after 4 h at 823 K. Carbon deposition occurred even under stoichiometrically excess steam-to-glycerol ratios. Carbon deposition increased significantly with increasing glycerol partial pressure in a non-linear fashion. In contrast, steam seemed to inhibit carbon laydown. Trimm [49] has reported similar inhibition on Ni-based catalysts with alkanes as the hydrocarbon substrate. Catalyst deactivation did not, however, appear to be problematic in the present study since the formation rates of H_2 and CO_2 were relatively stable throughout the reaction time.

4. Conclusions

The performance of Ni/Al_2O_3 catalyst for glycerol steam reforming has been investigated. NH_3 and CO_2-TPD analyses revealed that the catalyst surface was mainly populated by strong acid site. In particular, the reforming of glycerol occurred on this strong acidic site. H_2 and CO_2 formed the major products while CH_4 was mainly produced from the hydrogenolysis of glycerol. Methanation did not play any major role during the glycerol steam reforming as indicated by the product analysis of the reacting system. Arrhenius treatment of specific glycerol consumption rate gave activation energy estimation of approximately 60.0 kJ mol^{-1} for Ni/Al_2O_3 catalyst. Kinetic modelling of the experimental data, validated using MDC, parity and residual plots, showed that the rate behaviour may be adequately captured by a *Langmuir–Hinshelwood* (LH) model arising from molecular adsorption of glycerol and dissociative chemisorption of steam on two different sites (strong acid and basic sites) with surface reaction as rate determinant step. The characterization of used catalyst showed that carbon deposition was significant at 823 K, even under excess steam condition. The carbon deposition rate was proportional to the partial pressure of glycerol but inversely related to steam partial pressure.

Acknowledgements

We thank the Australian Research Council (ARC) for financial support. CKC would also like to acknowledge the University of New South Wales for a University International Postgraduate Award. SYF is grateful for an Australian Postgraduate Award.

References

[1] O. Senneca, Fuel Process. Technol. 88 (2007) 87.
[2] S. Turn, C. Kinoshita, Z. Zhang, D. Ishimura, J. Zhou, Int. J. Hydrogen Energy 23 (1998) 641.
[3] M. Ni, D.Y.C. Leung, M.K.H. Leung, K. Sumathy, Fuel Process. Technol. 87 (2006) 461.
[4] S. Rapagnà, N. Jand, P.U. Foscolo, Int. J. Hydrogen Energy 23 (1998) 551.
[5] J. Corella, M.P. Aznar, M.A. Caballero, G. Molina, J.M. Toledo, Int. J. Hydrogen Energy 33 (2008) 1820.
[6] Ø. Vessia, PhD Thesis, Norwegian University of Science and Technology, Trondheim (2005) 101.
[7] A. Dufour, P. Girods, E. Masson, Y. Rogaume, A. Zoulalian, Int. J. Hydrogen Energy 34 (2009) 1726.
[8] J.V. Gerpen, Fuel Process. Technol. 86 (2005) 1097.
[9] Y. Zhang, M. Dubé, D. McLean, M. Kates, Bioresour. Technol. 90 (2003) 229.
[10] A.V. Bridgwater, Chem. Eng. J. 91 (2003) 87.
[11] A.N. Fatsikostas, D.I. Kondarides, X.E. Verykios, Chem. Commun. (2001) 851.
[12] A.C. Basagiannis, X.E. Verykios, Int. J. Hydrogen Energy 32 (2007) 3343.
[13] A.N. Fatsikostas, D.I. Kondarides, X.E. Verykios, Catal. Today 75 (2002) 145.
[14] A.N. Fatsikostas, X.E. Verykios, J. Catal. 225 (2004) 439.
[15] T. Hirai, N.-O. Ikenaga, T. Miyake, T. Suzuki, Energy Fuels 19 (2005) 1761.
[16] J.D. Holladay, J. Hu, D.L. King, Y. Wang, Catal. Today 139 (2009) 244.
[17] N. Luo, X. Fu, F. Cao, T. Xiao, P.P. Edwards, Fuel 87 (2008) 3483.
[18] G. Wen, Y. Xu, H. Ma, Z. Xu, Z. Tian, Int. J. Hydrogen Energy 33 (2008) 6657.
[19] B. Zhang, X. Tang, Y. Li, Y. Xu, W. Shen, Int. J. Hydrogen Energy 32 (2007) 2367.
[20] R.R. Davda, J.W. Shabaker, G.W. Huber, R.D. Cortright, J.A. Dumesic, Appl. Catal. B 43 (2003) 13.
[21] M. Slinn, K. Kendall, C. Mallon, J. Andrews, Bioresour. Technol. 99 (2008) 5851.
[22] C.K. Cheng, S.Y. Foo, A.A. Adesina, Catal. Commun. 12 (2010) 292.
[23] K.M. Hardiman, PhD Thesis, The University of New South Wales, Sydney (2007) 397.
[24] J.C. Preece, PhD Thesis, The University of Birmingham, Birmingham (2005) 195.
[25] J.W. Shabaker, G.W. Huber, J.A. Dumesic, J. Catal. 222 (2004) 180.
[26] R.R. Davda, J.W. Shabaker, G.W. Huber, R.D. Cortright, J.A. Dumesic, Appl. Catal. B 56 (2005) 171.
[27] S. Adhikari, S. Fernando, A. Haryanto, Catal. Today 129 (2007) 355.
[28] S. Adhikari, S.D. Fernando, A. Haryanto, Renew. Energy 33 (2008) 1097.
[29] S. Adhikari, S.D. Fernando, S.D. Filip To, R.M. Bricka, P.H. Steele, A. Haryanto, Energy Fuels 22 (2008) 1220.
[30] A. Iriondo, V.L. Barrio, J.F. Cambra, P.L. Arias, M.B. Guemez, R.M. Navarro, M.C. Sanchez-Sanchez, J.L.G. Fierro, Top. Catal. 49 (2008) 46.
[31] I.N. Buffoni, F. Pompeo, G.F. Santori, N.N. Nichio, Catal. Commun. 10 (2009) 1656.
[32] L.P.R. Profeti, E.A. Ticianelli, E.M. Assaf, Int. J. Hydrogen Energy 34 (2009) 5049.
[33] A. Iriondo, V.L. Barrio, J.F. Cambra, P.L. Arias, M.B. Güemez, R.M. Navarro, M.C. Sanchez-Sanchez, J.L.G. Fierro, Catal. Commun. 10 (2009) 1275.
[34] E.A. Sánchez, M.A. D'Angelo, R.A. Comelli, Int. J. Hydrogen Energy 35 (2010) 5902.
[35] Praharso, A.A. Adesina, D.L. Trimm, N.W. Cant, Chem. Eng. J. 99 (2004) 131.
[36] D.L. Trimm, A.A. Adesina, Praharso, N.W. Cant, Catal. Today 93–95 (2004) 17.
[37] G.F. Froment, K.B. Bischoff, Chemical Reactor Analysis and Design, John Wiley & Sons, New York, 1990.
[38] T. Osaki, T. Mori, J. Catal. 204 (2001) 89.
[39] S. Natesakhawat, O. Oktar, U.S. Ozkan, J. Mol. Catal. A 241 (2005) 133.
[40] W. Brockner, C. Ehrhardt, M. Gjikaj, Thermochim. Acta 456 (2007) 64.
[41] G.A. El-Shobaky, N.M. Ghoneim, Thermochim. Acta 63 (1983) 39.
[42] R.H. Perry, D.W. Green, in: H. Robert, D.W. Perry, Green (Eds.), Perry's Chemical Engineer's Handbook, 7th ed., McGraw-Hill, New York, 1997.
[43] S. Adhikari, S. Fernando, A. Haryanto, Energy Fuels 21 (2007) 2306.
[44] C.C.R.S. Rossi, C.G. Alonso, O.A.C. Antunes, R. Guirardello, L.C.- Filho, Int. J. Hydrogen Energy 34 (2009) 323.
[45] C.L. Yaws (Ed.), Chemical Properties Handbook, McGraw-Hill, New York, 1999.
[46] H. Atia, U. Armbruster, A. Martin, J. Catal. 258 (2008) 71.
[47] W. Suprun, M. Lutecki, T. Haber, H. Papp, J. Mol. Catal. A: Chem. 309 (2009) 71.
[48] Y. Li, X. Wang, C. Xie, C. Song, Appl. Catal. A 357 (2009) 213.
[49] D.L. Trimm, Catal. Today 49 (1999) 3.